Carrier-Induced Band-Gap Variation and Point Defects in Zn_3N_2 from First Principles

Yu Kumagai,[1,2,*] Kou Harada,[3] Hirofumi Akamatsu,[3] Kosuke Matsuzaki,[1] and Fumiyasu Oba[3,1,4]

[1]*Materials Research Center for Element Strategy, Tokyo Institute of Technology, Yokohama 226-8503, Japan*

[2]*PRESTO, Japan Science and Technology Agency, Tokyo 113-8656, Japan*

[3]*Laboratory for Materials and Structures, Institute of Innovative Research, Tokyo Institute of Technology, Yokohama 226-8503, Japan*

[4]*Center for Materials Research by Information Integration, National Institute for Materials Science, Tsukuba 305-0047, Japan*

(Received 23 April 2017; published 14 July 2017)

The zinc nitride Zn_3N_2 is composed of inexpensive and earth-abundant Zn and N elements and shows high electron mobility exceeding 100 $cm^2\ V^{-1}\ s^{-1}$. Although various technological applications of Zn_3N_2 have been suggested so far, the synthesis of high-quality Zn_3N_2 samples, especially single crystals, is still challenging, and therefore its basic properties are not yet well understood. Indeed, the reported band gaps of as-grown Zn_3N_2 widely scatter from 0.85 to 3.2 eV. In this study, we investigate the large gap variation of Zn_3N_2 in terms of the Burstein-Moss (BM) effect and point-defect energetics using first-principles calculations. First, we discuss the relation between electron carrier concentration and optical gaps based on the electronic structure obtained using the Heyd-Scuseria-Ernzerhof hybrid functional. The calculated fundamental band gap is 0.84 eV in a direct-type band structure. Second, thermodynamic stability of Zn_3N_2 is assessed using the ideal-gas model in conjunction with the rigid-rotor model for gas phases and first-principles phonon calculations for solid phases. Third, carrier generation and compensation by native point defects and unintentionally introduced oxygen and hydrogen impurities are discussed. The results suggest that a significant BM shift occurs mainly due to oxygen substitutions on nitrogen sites and hydrogen interstitials. However, gaps larger than 2.0 eV would not be due to the BM shift because of the Fermi-level pinning caused by acceptorlike zinc vacancies and hydrogen-on-zinc impurities. Furthermore, we discuss details of peculiar defects such as a nitrogen-on-zinc antisite with azidelike atomic and electronic structures.

DOI: 10.1103/PhysRevApplied.8.014015

I. INTRODUCTION

Nitrides possess various advantages for practical use as semiconductors. The constituent nitrogen is abundant and nontoxic. Moreover, since higher energy levels of N $2p$ states than of O $2p$ ones lead to higher valence-band maxima (VBM), nitrides can be doped into p type even without large cationic orbital contributions such as Cu $3d$ and Sn $5sp$ [1,2]. It also makes the band gaps narrower than oxides, which makes some nitrides suitable for light-absorbing layers of photovoltaic solar cells and photoelectrochemical cells [2]. Thus, various nitride semiconductors and their alloys have been reported and investigated aiming at a variety of applications such as optoelectronics, photovoltaics, power devices, and so on [2–12].

The foremost important nitrides are GaN and alloys based upon it that have been developed for commercial optoelectronic devices [7–9]. Other nitrides have been much less investigated but are currently attracting growing research interest. In particular, thanks to recent progress in crystal growth techniques, high-quality nitride samples—including metastable ones—can now be prepared. One of the attractive nitrides is Zn_3N_2 [13], whose biggest advantage is its high electron mobility, which exceeds 100 $cm^2\ V^{-1}\ s^{-1}$ [14–17] (the record is 395 $cm^2\ V^{-1}\ s^{-1}$ [15]). There have been reports suggesting the use of Zn_3N_2 as transparent conductors [18], channel layers for optoelectronic devices [19], negative electrodes in Li-ion batteries [20], and precursor films for p-type doped ZnO [21]. Thus far, Zn_3N_2 samples have been synthesized using various techniques, such as pulsed-laser deposition [22,23], molecular beam epitaxy [15,16,24], chemical vapor deposition [16,25], electrochemical processes [26], sputtering [17,27–30], and ammonolysis reactions [31–33]. However, synthesis of high-quality Zn_3N_2 samples, especially single crystals, is

*yuuukuma@gmail.com

still challenging, presumably due to its nearly zero formation enthalpy [34], and hence its basic properties are not yet well understood.

The most controversial but technologically important physical property of Zn_3N_2 is the band gap. The reported band gaps of as-grown Zn_3N_2 range from 0.85 to 3.2 eV [14–16,26,28–31,33,35,36]. Indeed, experimental gaps of some other nitride semiconductors notoriously scatter as well. The most memorable example is InN; for several decades, its gap had been believed to be around 2.0 eV, but it was revised to 0.6–0.7 eV after 2002 [37–39]. The same case holds for ScN and $ZnSnN_2$; the reported gap ranges are 0.9–1.5 and 1.4–2.9 eV, respectively [11,40]. Such large variations are attributed mainly to the Burstein-Moss (BM) effect [41,42], where the carrier concentration is so high that the Fermi level shifts into the host valence or conduction band, leading to extended optical gaps. Some experimental studies have demonstrated that the optical gaps of nitrides change as a function of carrier electron concentration. The experimental results of InN, GaN, ScN, and $ZnSnN_2$ have also been examined by using first-principles calculations in terms of the BM effect [11,39,40].

Likewise, the BM effect has been considered as the most likely cause for the wide variety of reported gaps for Zn_3N_2, although the variation range is much larger than those of other nitrides. Another suggested possibility includes oxygen impurities leading to a larger ionicity, which may cause wider band gaps [28,36]. Besides, most Zn_3N_2 samples have been found to be unintentionally *n* type with a carrier concentration of 10^{18}–10^{20} cm^{-3}. It is widely accepted that nitrogen vacancies and/or oxygen substitutions at nitrogen sites are responsible for the generation of such high carrier electrons [16,18,19,27,30,36]. However, there is still no clear theoretical support; researchers have investigated native defects [43], oxygen impurities [44], and copper, silver, and gold dopants [45] in Zn_3N_2 in the neutral charge state using first-principles calculations. However, they adopted the local-density approximation (LDA) and/or the generalized-gradient approximation (GGA), both of which predict Zn_3N_2 to be (nearly) metallic and so are not suited for predicting defect properties even qualitatively. Furthermore, calculations of charged defects are essential for identifying the source of the carrier electrons [46]. Such calculations can also provide insight into the possibility of controlling a carrier electron concentration in Zn_3N_2, which is indispensable for device applications such as transistors.

In this paper, our main purpose is twofold. First, we discuss the relation between the electron carrier concentration N_e and the optical gap determined from absorption processes E_g^{opt} based on the calculated band structure and density of states (DOS) (Sec. III B). We use the Heyd-Scuseria-Ernzerhof (HSE06) hybrid functional, which has been reported to accurately predict the band gaps of semiconductors, especially nitrides [11,12,40]. We also compare our results with measured E_g^{opt} as a function of N_e. Second, we show the calculation results of native point defects and unintentionally introduced oxygen and hydrogen into Zn_3N_2 (Sec. III D). Image-charge interactions under periodic boundary conditions are corrected by using our extended Freysoldt–Neugebauer–Van de Walle (FNV) scheme, which is verified through a series of different supercell calculations with GGA with the Hubbard *U* correction (see the Appendix) [47]. Such defect calculations allow us to reveal the dominant point defects generating the carrier electrons and, therefore, causing the BM shift. In addition, we also discuss the variable range of the Fermi level in view of the Fermi-level pinning. Furthermore, it is well known that nitrides tend to be thermodynamically less stable than oxides. Thus, in Sec. III C, we examine the thermodynamic stability of Zn_3N_2 using the ideal-gas model in conjunction with the rigid-rotor model for gas phases and first-principles phonon calculations for solid phases. This analysis also provides the chemical potentials used in the discussion of defect energetics.

II. METHODS

A. Computational details

The calculations are performed using the projector augmented-wave (PAW) method [48] as implemented in the Vienna *ab initio* simulation package [49,50]. PAW data sets with radial cutoffs of 1.22, 0.79, 0.80, and 0.58 Å for Zn, N, O, and H, respectively, are employed. Zn $3d$ and $4s$, N $2s$ and $2p$, O $2s$ and $2p$, and H $1s$ orbitals are considered as valence electrons. For the perfect crystal, the lattice constant and the internal atomic positions are fully optimized until the residual stresses and forces converge to less than 0.01 GPa and 0.01 eV/Å, respectively. In this study, we adopt the HSE06 hybrid functional [51–53], which describes the electronic structures of semiconductors more accurately than LDA or GGA [53–56] and has been applied to their point defects [12,57–60]. The screening parameter and mixing of Hartree-Fock exchange are set at the HSE06 values of 0.208 $Å^{-1}$ and 0.25 [53]. Defect calculations are performed at the theoretical lattice constant of perfect Zn_3N_2. The internal atomic positions are relaxed until the residual forces reduce to less than 0.04 eV/Å. Wave functions are expanded with a plane-wave basis set. Cutoff energies are set to 550 and 400 eV for the calculations of perfect Zn_3N_2 and defective systems, respectively. Spin polarization is considered for all of the defects.

B. Thermodynamic stability

In this study, we discuss the thermodynamic stability of Zn_3N_2 at finite temperatures. The entropic contributions of N_2 and NH_3 are obtained using the ideal-gas model in conjunction with the rigid-rotor model [61].

The characteristic rotational temperatures and vibrational temperatures measured by experiments are taken from Ref. [61]. For solid phases of antibixbyite Zn_3N_2, wurtzite ZnO, and hexagonal close-packed Zn, we calculate the Gibbs free energies within the quasiharmonic approximation [62]. The PBEsol functional (the Perdew-Burke-Ernzerhof functional parametrized for solids) [63] is employed for the calculations of cell-volume-dependent phonon frequencies. For insulating Zn_3N_2 and ZnO, on-site Coulomb interactions on the Zn $3d$ states are taken into account by the $+U$ correction according to Dudarev's formalism [64]. The effective U value $U_{\mathrm{eff}} = U - J$ is set at 5 eV, with which the Zn $3d$ band position with respect to the VBM is very close to that calculated by the HSE06 functional [55]. We use $2 \times 2 \times 2$ supercells for Zn_3N_2 and $3 \times 3 \times 2$ supercells for ZnO and Zn. The cell volume is varied in the range of about 85% to 115% of the equilibrium volume, depending on the compounds. At the various cell volumes, the atomic coordinates are optimized until the forces converge to less than 0.001 eV/Å, and finite displacements are then introduced. Using the PHONOPY code [65], the phonon frequencies are computed from the calculated force constants. The Gibbs free energies at zero pressure and given temperatures are derived via minimization of Helmholtz free energies with respect to volume.

C. Point defects

The formation energy of a point defect is calculated as [47]

$$E_f[D^q] = (E[D^q] + E_{\mathrm{corr}}[D^q]) - E_P - \sum n_i \mu_i + q(\epsilon_{\mathrm{VBM}} + \Delta\epsilon_F), \quad (1)$$

where $E[D^q]$ and E_P are the total energies of the supercell with defect D in charge state q and the perfect-crystal supercell without any defect, respectively. n_i is the number of removed ($n_i < 0$) or added ($n_i > 0$) i-type atoms and μ_i refers to the chemical potential. The chemical potentials depend on the growth condition, which is discussed in detail in Sec. III C. ϵ_{VBM} is the energy level of the VBM in perfect Zn_3N_2. $\Delta\epsilon_F$ represents the Fermi level with respect to the VBM. Note that, when discussing the BM effect, $\Delta\epsilon_F$ not only varies inside the band gap but also moves into the conduction band. Therefore, we need to take special care for the defect calculations, which are dealt with in Sec. III D 1. Except for the exchange-correlation functional approximated, an error in the defect-formation energy mainly comes from the spurious electrostatic interactions under periodic boundary conditions. $E_{\mathrm{corr}}[D^q]$ corresponds to its correction energy. We emphasize that the potential alignment is not considered because it is unnecessary when the image-charge correction is properly applied [47]. We estimate $E_{\mathrm{corr}}[D^q]$ using our extended FNV scheme, which can correct energies of charged defects accurately [47,66,67]. Based on the careful cell-size test, we adopt the primitive cell with 40 atoms for defect calculations (see the Appendix for details). The defect eigenvalues are also corrected within the point-charge approximation as discussed in Refs. [58,68].

III. RESULTS AND DISCUSSION

A. Fundamental properties of the perfect crystal

Figure 1 presents the crystal structure of the cubic antibixbyite Zn_3N_2 with the space group of $Ia\bar{3}$, which can also be regarded as a defective antifluoride structure. As seen, each Zn atom is surrounded by four N atoms, and each N atom by six Zn atoms. The calculated theoretical lattice constant is 9.76 Å, agreeing very well with the experimental values of 9.77–9.78 Å [31–33].

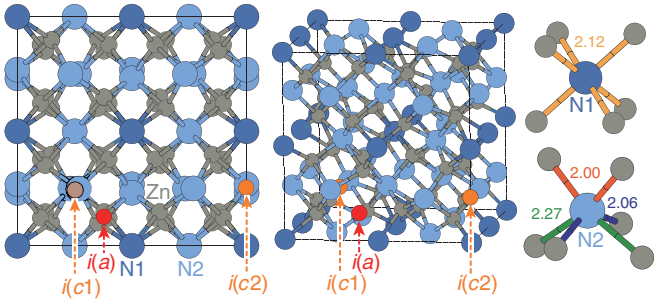

FIG. 1. Antibixbyite crystal structure of Zn_3N_2. The conventional unit cell shown includes 80 atoms, whereas the primitive cell 40 atoms. The small gray balls represent Zn atoms, and the large blue ones N atoms. Two inequivalent nitrogen sites are distinguished as N1 ($8b$) and N2 ($24d$). The bond distances from neighboring Zn are also shown in Å and equivalent bonds are grouped using the same colors. For the defect calculations, interstitial sites coordinated by cation zinc atoms (two inequivalent sites) and anion nitrogen atoms are considered; they are depicted as $i(c1)$, $i(c2)$, and $i(a)$.

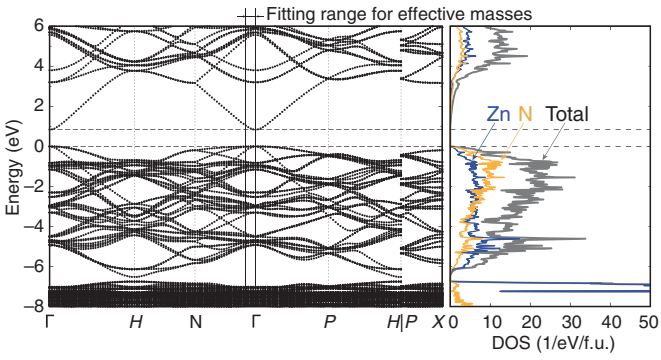

FIG. 2. Calculated band structure and DOS of Zn_3N_2 using the HSE06 functional at the theoretical lattice constant. The zero of energy is set at the VBM. The horizontal dashed lines indicate the VBM and conduction-band minimum (CBM), located at the Γ point. The band path is taken from Ref. [69]. The partial DOSs of Zn and N are summed from all of the Zn sites and N sites, respectively. The fitting range used for estimating the effective masses in this study is also shown.

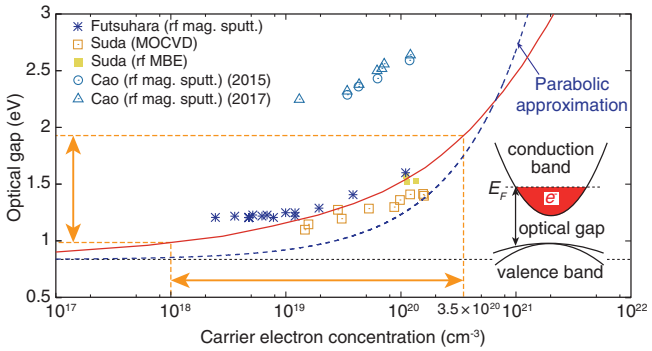

FIG. 3. Optical gap determined from absorption processes as a function of carrier electron concentration estimated from the band structure and the DOS computed with the HSE06 functional (see the text for details). The same information calculated within the parabolic band approximation is shown by a dashed line (see the text for details). A horizontal dotted line indicates the calculated fundamental gap. The compiled experimental data measured from samples grown by metal-organic chemical vapor deposition (MOCVD), molecular beam epitaxy (MBE), and radio-frequency magnetron sputtering (rf mag. sputt.) are also shown by points [14,16,18,70]. A horizontal arrow shows a range of experimentally reported electron carrier concentration, and a vertical one the range of the corresponding optical gaps. Note that the variation of the optical gap is mainly attributed to the shift of the Fermi level, as the change in the valence band is very small along the Γ-N line (see Fig. 2). For instance, the difference between the changes of the optical gap and the Fermi level is 0.05 eV at an electron carrier concentration of 3.5×10^{20} cm^{-3}.

Figure 2 shows the calculated band structure and DOS of Zn_3N_2. The band structure shows a direct gap at the Γ point. The fundamental gap is estimated at 0.84 eV, consistent with the reported HSE06 gap of 0.86 eV [55]. We previously found that the HSE06 functional performs better than the GW_0 approximation for predicting the band gaps of several nitrides [12]. Deng *et al.* [40] and Lahourcade *et al.* [11] have also reported that the HSE06 functional can more accurately predict the experimental gaps of ScN and $ZnSnN_2$, respectively, than the *GW* approximations. Thus, the fundamental gap of pristine Zn_3N_2 is expected to be approximately 0.84 eV. The site-projected DOS shows strong hybridization between the closed-shell Zn 3*d* and N 2*p* states in the valence band, which is expected to reduce the hole effective mass compared to other nitrides [12]. Actually, in addition to a very low electron effective mass m_e of $0.08m_0$ originating from unoccupied Zn 4*s* states, where m_0 means the free-electron rest mass, the effective mass of the heavy hole m_h of $0.99m_0$ is nearly half of GaN [12].

B. Carrier-induced optical-gap variation

In Fig. 3, we show an optical gap determined from absorption processes $E_g^{\rm opt}$ as a function of electron carrier concentration N_e calculated from the band structure and DOS in Fig. 2. For estimating $E_g^{\rm opt}$, we should keep the following in mind: (1) The electronic transition from the highest valence band to the lowest conduction band is dipole allowed. (2) Since only a vertical transition is optically allowed when the phonon-assisted transition is ignored, the valence-band curvature needs to be taken into account (see the inset of Fig. 3). Thus, $E_g^{\rm opt}$ is computed by the following two steps: First, a relation between the Fermi-level position in the conduction band and N_e is calculated from the DOS. Then, we calculate a relation between $E_g^{\rm opt}$ and the Fermi-level position from the band structure. Note that the temperature effect is ignored in this subsection because we have found that it is small compared to the energy scale discussed here.

We also calculate $E_g^{\rm opt}$ against N_e within the parabolic approximation frequently used for the analysis of experimental data by adding

$$\Delta E = \frac{\hbar^2}{2}\left(\frac{1}{m_e}+\frac{1}{m_h}\right)(3\pi^2 N_e)^{2/3} \tag{2}$$

to the fundamental gap of 0.84 eV. Note that this equation is derived from the free-electron model and leads to the well-known relationship $\Delta E \sim N_e^{2/3}$. The carrier effective masses depend on the region for fitting the band structure. Here, we adopt the band along the Γ-N direction giving the heaviest effective hole mass, with a relatively longer distance of 1.16 Å^{-1} (Fig. 2), which gives $m_e = 0.20m_0$ and $m_h = 8.21m_0$. The discrepancy from the effective masses in Ref. [12] is attributed to the difference of the fitting range and direction. Indeed, when the masses are evaluated in the vicinity of the band edges, we obtain $m_e = 0.08m_0$ and $m_h = 0.99m_0$, which are the same as reported values in the literature [12].

One can see that our calculated $E_g^{\rm opt}$ against N_e accurately reproduces the experimental reports by Suda and Kakishita [16] and Futsuhara *et al.* [14]. Conversely, the parabolic approximation relatively fails to match up with the experiments. The discrepancy between directly calculated $E_g^{\rm opt}$ and that of the parabolic approximation is not so small. This is because the conduction band varies not quadratically but nearly linearly from the Γ point to nearby special points in the relevant energy range, as seen in Fig. 2. It has also been reported that the parabolic approximation does not work well for InN either [38].

The reported carrier concentrations lie mostly in the range 10^{18}–3.5×10^{20} cm^{-3} [14–17,28,35,36], which correspond to band gaps of 1.0–1.9 eV, as shown in Fig. 3. Obviously, gaps larger than 2.0 eV depart from our calculated $E_g^{\rm opt}$, and other experimental values by about 1 eV. Furthermore, because of the Fermi-level pinning caused by acceptor-type defects, as is shown in Sec. III D, it should be difficult to lift the Fermi level to higher than

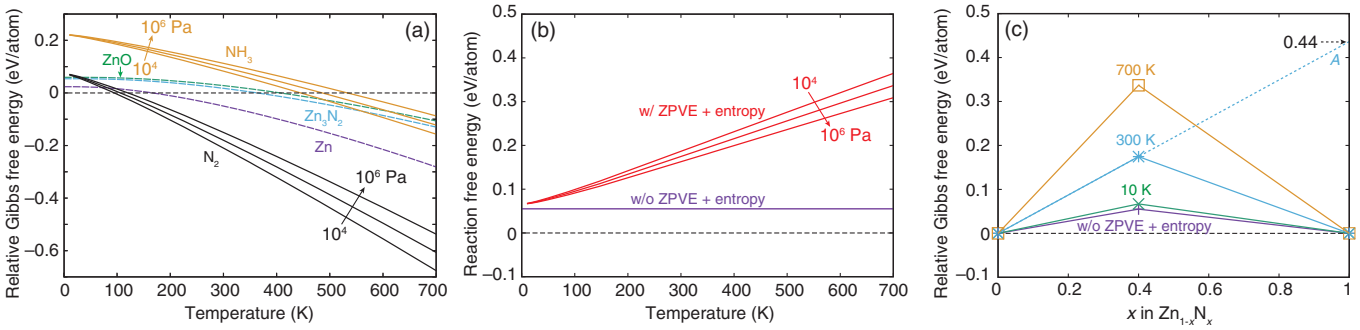

FIG. 4. (a) Temperature dependence of sums of the zero-point vibrational energies (ZPVE) and entropy contributions to the Gibbs free energies. The values of solids (the dashed lines) are calculated using the PBEsol$(+U)$ functional (see the text for details), whereas those for gas phases (the solid lines) are quantified based on the characteristic rotational temperatures and vibrational temperatures. The pressures of the gas phases are set to 10^4, 10^5, and 10^6 Pa. (b) Gibbs free energy of formation of Zn_3N_2, i.e., the free energy of reaction, $3Zn + N_2 \rightarrow Zn_3N_2$. Note that the total energy contributions are calculated using the HSE06 functional. (c) Calculated Gibbs free energies of Zn_3N_2 with respect to Zn and N_2 at 10, 300, and 700 K estimated from (b). The intersections between the dotted line A and the y axes correspond to Zn and N chemical potentials at the condition where Zn_3N_2 is grown at the Zn-rich condition at 300 K.

1.0 eV from the CBM, corresponding to $E_g^{\mathrm{opt}} = 1.9$ eV. We return to a discussion of such large optical gaps in Sec. III D.

It is also known that the band-gap renormalization may be significant when such a high concentration of carrier electrons is introduced. Therefore, we calculate its effect by adding electrons into pristine Zn_3N_2 up to 3.3×10^{20} cm^{-3}, which is nearly the maximum value of the electron carrier concentration reported. As a result, we find that the variation of the fundamental band gap is only 0.08 eV, whereas the variation caused by the BM shift is more than 1 eV. Thus, the renormalization effect would not be significant in Zn_3N_2.

C. Thermodynamic stability of Zn_3N_2 and chemical potentials of the related compounds

In this subsection, we discuss thermodynamic stability of Zn_3N_2. It is well known that nitrides are difficult to grow compared to oxides. This is mainly due to the strong stability of the N_2 molecule with a triple bond. Discussions of the stability of nitrides at finite temperatures based on first-principles calculations have not been common in the past. Here, we report it by taking Zn_3N_2 as an example.

Figure 4(a) shows sums of zero-point vibrational energies and entropy contributions to the Gibbs free energies for Zn_3N_2, Zn, N_2, ZnO, and NH_3 as a function of temperature; the latter two are later used for determining the chemical potentials of O and H. By adding these contributions to the total energies, the Gibbs free energies are obtained. One can see that the phonon contributions in solids are small at around room temperature (< 0.1 eV) as a result of cancellation of the zero-point vibrational energies and phonon entropy contributions. The variation of the free energy is highest for the N_2 gas phase because the entropic contribution by the translation degree of freedom per atom is high.

The Gibbs free energy of formation for Zn_3N_2 as a function of temperature at $p_{N_2} = 10^5$ Pa is shown in Fig. 4(b). Note that the total energies are calculated using the HSE06 functional, and the phonon frequencies of the solids from PBEsol$(+U)$ as described in Sec. II B. As seen, Zn_3N_2 is thermodynamically unstable in a whole range of temperatures and becomes less stable as increasing temperature. Indeed, the growth of nitrides is usually cumbersome and typically requires the experimental techniques that can achieve higher nitrogen chemical potential than that of the N_2 gas phase at the standard state, such as molecular beam epitaxy, ammonolysis reaction, and high-pressure synthesis [2]. However, once the nitrides are synthesized, they can be kinetically stable thanks to the strong chemical bonding between cations and nitrogen ions [2].

D. Point defects

Here, we discuss formation energies and thermodynamic transition levels (TTLs) of native point defects and unintentionally doped oxygen and hydrogen in Zn_3N_2. We consider the vacancies, antisites, and interstitials shown in Fig. 1 for native defects, and substitutional and interstitial sites for oxygen and hydrogen impurities. A wide range of charge states is considered for each defect, and symmetry constraints are removed.

1. Procedure of defect calculations at the Fermi level located above the CBM

In this study, we want to identify dominant defects introducing carrier electrons and causing the BM shift. To this end, we need to calculate the defect-formation energies and TTLs at the Fermi level, which are a few eV above the CBM. This conclusion is, however, not possible when the k-point sampling mesh covers the band edges. More specifically, let us think about Zn_3N_2, in which the VBM and CBM locate at the Γ point. When the Γ point is included in the k-point sampling, a filled electronic state existing above the CBM releases electrons to the CBM

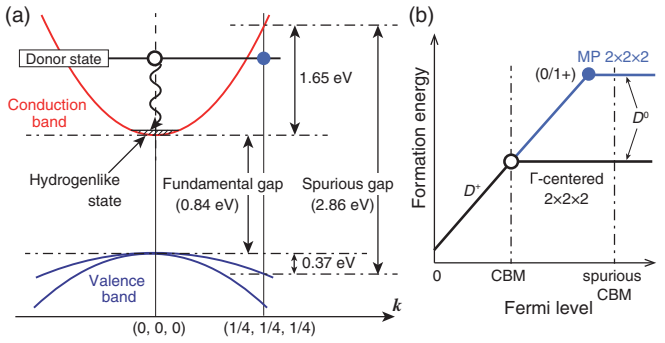

FIG. 5. Schematic illustrations of (a) the band structure of Zn_3N_2 and (b) the formation energies of donorlike defect D. Note that when a $2 \times 2 \times 2$ MP mesh is used, the computed band gap is spuriously increased, and the TTLs are calculated appropriately within the spurious gap (see the text for details).

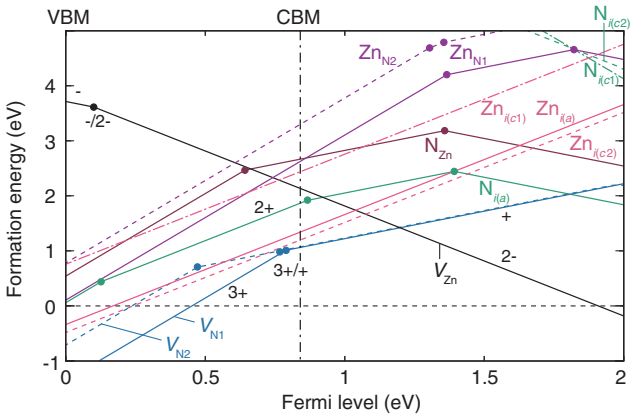

FIG. 6. Formation energies of native point defects in Zn_3N_2 as a function of the Fermi level, ranging from the VBM, which is set to zero, to 2 eV so that the BM shift is discussed. V's in defect species denote vacancies, and the subscripts defect sites, where i indicates interstitial sites. The charge states of defects correspond to the gradients. Only the most energetically favorable charge state at a given Fermi level is shown for each defect. Positive and negative charge states indicate donor and acceptor behavior, respectively. The Fermi level at which the favorable charge state changes corresponds to the positions of the donor or acceptor levels, which are designated by filled circles.

and forms a hydrogenlike state, as illustrated in Fig. 5(a). In such a case, the TTL is located adjacent to the CBM [Fig. 5(b)], which is not appropriate when the Fermi level moves above the CBM. Thus, we instead use a $2 \times 2 \times 2$ Monkhorst-Pack (MP) k-point sampling mesh [71] for point-defect calculations, which excludes the Γ point. The band gap is then spuriously increased as depicted in Fig. 5(a), and, consequently, the TTLs of the donor states are properly calculated at the Fermi level, being within the spurious gap. The same procedure was also employed by Janotti *et al.* for the study of point defects in InN [72]. Since the spurious CBM locates at 2.49 eV above the fundamental VBM when using the HSE06 functional, we show the defect-formation energies up to $\Delta\epsilon_F = 2.0$ eV in this study.

2. Native point defects

Figure 6 shows a plot of calculated formation energies for native point defects against the Fermi level in Zn_3N_2. Since Zn_3N_2 is unstable compared to Zn metal and N_2 gas at the entire temperature range, as discussed in Sec. III C, we set the chemical potentials at the condition where Zn and Zn_3N_2 coexist at 300 K [denoted as A in Fig. 4(c)]. This situation is proximate to the Zn-rich equilibrium condition, which is usually considered for defect calculations.

It is noteworthy that all of the defects except for zinc vacancies (V_{Zn}) behave as donors when the Fermi level is within the fundamental gap. Among the donors, nitrogen vacancies (V_N) at the N1 site have the lowest formation energies. However, the other defects may also be present in large numbers if we can increase μ_N as discussed in Ref. [2]. Although $V_{N1}{}^{+}$ and $V_{N2}{}^{+}$ show nearly the same formation energies, their 3+ charge states, being dominant for Fermi-level positions in the fundamental gap, are very different. Indeed, Paniconi *et al.* reported that neutron-diffraction data indicate that the N1 site shows lesser site occupancy than the N2 site in their samples, with relatively low experimental band gaps of approximately 0.9 eV [33]. Neither $V_{N1}{}^{2+}$ nor $V_{N2}{}^{2+}$ appear in Fig. 6, meaning their negative-U characteristics that is common for anion vacancies [73]. On the other hand, V_{Zn} becomes a shallow acceptor center, in contrast to V_{Zn} in ZnO with deep acceptor levels [57,74], and constructs a Fermi-level pinning at $\Delta\epsilon_F = 1.9$ eV, from which the Fermi level cannot be lifted due to the spontaneous generation of acceptor V_{Zn}.

Among the interstitials, nitrogen interstitials (N_i) show unusual behaviors in view of the ionic picture. First, $N_{i(c1)}$ and $N_{i(c2)}$ are very high in energy, although the $i(c1)$ and $i(c2)$ sites are surrounded by Zn cations. By contrast, $N_{i(a)}$ shows much lower energy and acts as a donor center at $E_F < 1.5$ eV. This is counterintuitive because N atoms usually attract electrons as anions. To take a closer look, we investigate the atomic and electronic structures of $N_{i(a)}$ as shown in Figs. 7 and 8. One can see that $N_{i(a)}$ locates near a host N atom with a strong bond in all charge states; the N-N distances are close to that of a N_2 molecule, indicating that $N_{i(a)}$ comprises a diatomic molecule. N $2p$ orbitals of the N_2 molecule form a triple bond, i.e., σ and π bonds, and σ^* and π^* antibonds, as shown in Fig. 8. The σ and π bonds of the N_2 dimerlike defect locate about 10 and 12 eV below the VBM of Zn_3N_2 and the σ^* bond about 5 eV above the CBM. On the other hand, the π^* bonds exist around the band edges when occupied, and three electrons originating from the host N^{3-} are located at π^*. Thus, one more electron can be added to π^* and three electrons can be removed. Consequently, $N_{i(a)}$ can be mainly in the $-$, $+$,

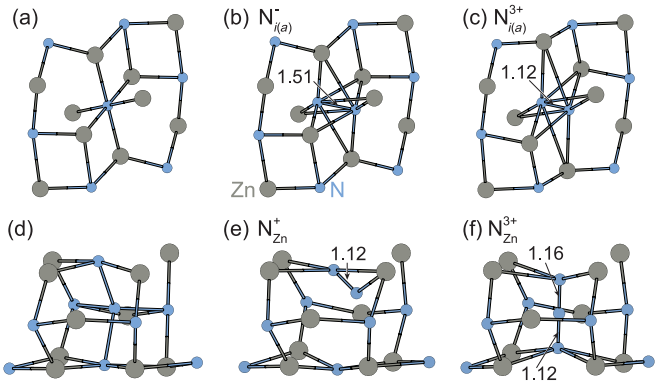

FIG. 7. Local atomic structures of (a) perfect Zn_3N_2, (b),(c) $N_{i(a)}$ in the − and 3+ charge states, (d) N_{Zn} before geometry optimization, and (e),(f) N_{Zn} in the + and 3+ charge states. The N—N bond distances are also shown in Å. Note that the calculated N—N bond distances in N_2 and N_3^- molecules by the HSE06 functional are 1.11 and 1.18 Å.

2+, or 3+ charge states, as shown in Fig. 6. Furthermore, as more electrons are donated to π^*, the N—N bonds are weakened more and become longer. Regarding zinc interstitials (Zn_i), $Zn_{i(c2)}$ finally transitions to the $i(a)$ site via geometry optimization, and it is not shown in Fig. 6. Both $Zn_{i(c1)}$ and $Zn_{i(a)}$ take the 2+ charge state in a wide Fermi-level range, and $Zn_{i(a)}$ is lower in energy, probably thanks to the attractive electrostatic interaction from nearby N^{3-} ions, and can be present in significant concentration at a lower Fermi level.

Zinc-on-nitrogen antisites (Zn_N) show higher energies and are not important in Zn_3N_2. On the contrary, nitrogen-on-zinc antisites (N_{Zn}) have lower formation energies and are donors at a lower Fermi level, which is also not compatible with the ionic view. Figures 7 and 8 show the atomic and electronic structures of N_{Zn}. Intriguingly, it is seen that N_{Zn}^{3+} constructs a linear bond with two N atoms, namely, an azidelike structure. The bond distances between the N atoms shown in Fig. 7 are also very close to that of the azide N_3^- molecule. When constructing the azidelike structure, six electrons spill out from two host N^{3-} ions. Among these electrons, one and two electrons move to N_3^- and V_{Zn}^{2-}, respectively, and three electrons remain. Therefore, the azidelike N_{Zn} defect takes the 3+ charge state. Conversely, N_{Zn} in the 2+ or lower charge state forms a N—N bond with a nearby N atom, as in the case of $N_{i(a)}$.

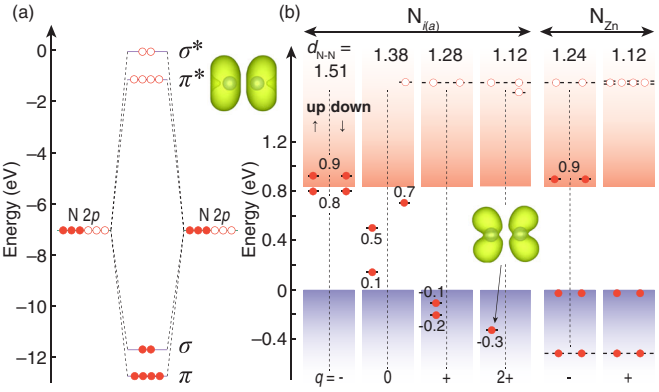

FIG. 8. (a) Calculated orbital levels of a N atom and a N_2 molecule using the HSE06 functional. The energies are shown with respect to the vacuum level. Although N 2*s* orbitals hybridize with σ and σ^*, this is not explicitly stated here for the sake of simplicity. (b) Spin-resolved-defect-induced single-particle levels of $N_{i(a)}$ and N_{Zn}. Note that $N_{i(a)}^{3+}$ and N_{Zn}^{3+} do not have in-gap states, so they are not shown here. The dashed lines indicate the deep levels located outside the spurious band gap before applying corrections for the defect eigenvalues (see the text for details).

3. *Oxygen and hydrogen impurities*

Oxygen has been considered to be a prime source of the BM effect in Zn_3N_2. Hydrogen is also commonly unintentionally incorporated into nitrides and becomes donor centers, although it is not yet regarded as a source of the BM effect in Zn_3N_2. Therefore, we investigate their behaviors as impurities in Zn_3N_2.

Figure 9 shows calculated formation energies for oxygen impurities in Zn_3N_2. The chemical potential of O is determined at the condition where Zn and ZnO coexist at 300 K [see Fig. 4(a)]. The results show that O atoms preferentially locate at the nitrogen sites and show single donor states. The oxygen-on-nitrogen defects (O_N) have significantly lower formation energies than V_N at a higher Fermi level. Near O_N^+, the Zn—O bonds are about 0.1 Å longer than the original Zn—N bonds, although the ionic radius of O is slightly smaller than that of N. (The ionic radius of four-coordinated O^{2-} is 1.24 Å, whereas that of N^{3-} is 1.32 Å [75].) This is because the ionic attraction by

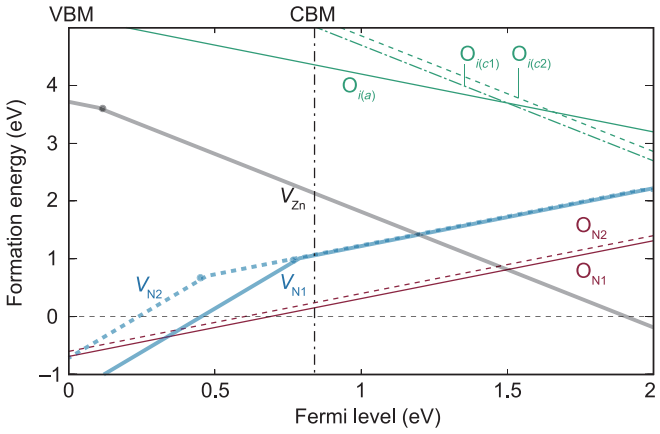

FIG. 9. Same as in Fig. 6, but for oxygen impurities. The formation energies of native defects with lower energies, i.e., vacancies, are also shown for comparison.

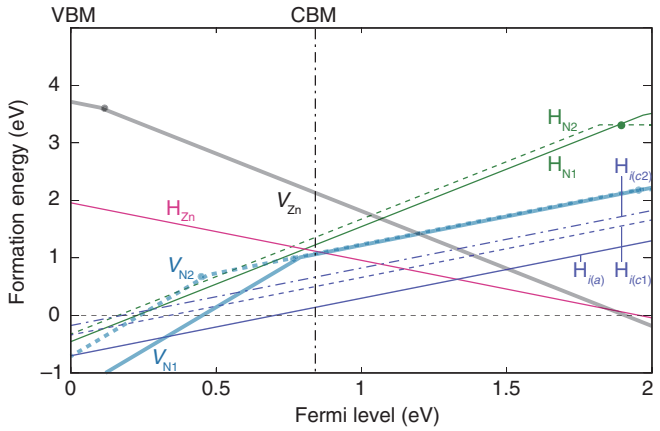

FIG. 10. Same as in Fig. 9, but for hydrogen impurities.

O^{2-} is weaker than that by N^{3-}. On the other hand, O atoms at the interstitial sites (O_i) are acceptors but are very high in energy.

Figure 10 presents a plot of formation energies for hydrogen impurities. According to the Open Quantum Materials Database [76], Zn_3N_2 competes with Zn, NH_3, and N_2 molecules in the Zn-N-H ternary phase diagram at 0 K, when Zn_3N_2 is assumed to be slightly stable with respect to Zn and N_2. Thus, the chemical potential of H is determined at the condition where Zn, Zn_3N_2, and NH_3 coexist at 300 K and $p_{NH_3} = 10^5$ Pa. The results show that hydrogen atoms preferentially locate at the $i(a)$ sites in the + charge state, and its energy is very low and even comparable to O_N. Hydrogen-on-zinc defects (H_{Zn}) show acceptor behaviors and a slightly higher pinning level compared to V_{Zn}. H atoms in the H_{Zn}, $H_{i(a)}$, $H_{i(c1)}$, and $H_{i(c2)}$ defects show protonic characteristics and strongly bind to a neighboring N atom with N─H bond distances of 1.02–1.04 Å, which are very close to that of the NH_3 molecule (1.01 Å by the HSE06 functional). Hydrogen-on-nitrogen defects (H_N) are mostly double donors. We analyzed their atomic and electronic structures and have found that H_{N1} stays at the symmetric substitutional site with constructing the so-called hydrogen multicenter bonding as in InN [77]. On the other hand, H_{N2} shows a similar tendency but locates near two Zn atoms with a localized state. As a result, H_{N2} shows the $2+/0$ transition level at 1.9 eV. These defects, however, are higher in energy than H_i in the *n*-type regime.

The point-defect calculations shown ensure that the BM shift in Zn_3N_2 is mainly attributed to $O_N{}^+$ and/or $H_{i(a)}{}^+$, rather than V_N. This conclusion is the same as that of InN [77]. If, however, the nitrogen chemical potential is increased as discussed in Ref. [2], the energy of V_N increases, whereas the energy of V_{Zn} decreases. As a consequence, the Fermi level can be dropped near the CBM, which might happen when Zn_3N_2 with a relatively low optical gap is grown.

E. Origin of larger experimental optical gaps

Based on our theoretical calculations, it seems difficult to lift the Fermi level over 2.0 eV from the VBM in view of the Fermi-level pinning caused by V_{Zn} and H_{Zn}. In addition, we need to introduce electrons in a high concentration such as 5×10^{20} cm^{-3} for band gaps larger than 2 eV (see Fig. 3). Thus, such high band gaps are not attributed to the BM effect. Here, we discuss alternative possibilities to explain the larger optical gaps observed in experiments.

First, we consider the possibility that charged defects increase the fundamental gaps. This is called band-gap renormalization (BGR), although it usually decreases the band gaps. To check this effect, we calculate the fundamental gaps of the models with the dominant defects $O_{N1}{}^+$, $O_{N2}{}^+$, and $H_{i(a)}{}^+$, but we find that these reduce the fundamental gaps by less than 0.1 eV. Therefore, BGR is not considered to be a source of the large gaps.

Another possibility is that samples are not pristine Zn_3N_2 but partly include zinc oxide and/or oxinitride phases. To check this possibility, we calculate a model in which one Zn atom in the primitive cell is removed and two neighboring N atoms are replaced by O atoms. Note that charge neutrality is preserved in this model as $V_{Zn}{}^{2-} + 2O_N{}^+$ is introduced. The fraction of oxygen at anion sites is then $O/(O+N) = 2/16 = 12.5\%$, which is slightly higher than those of intentionally oxygen-doped samples made by Cao *et al.* [18]. The calculated fundamental gap of this model is 0.91 eV, which is only 0.07 eV higher than that of pristine Zn_3N_2. Thus, small fraction of alloying with ZnO is not a cause of the large gaps. However, if a majority of the sample is oxidized to ZnO, $Zn(OH)_2$, or their mixed phase, the band gaps are drastically changed, as discussed by Trapalis *et al.* [36].

The third possible origin is the uncertainty of the fitting of the absorption spectra. Most groups have estimated band gaps by extrapolating the optical absorption spectra with a Tauc plot with an expression of $(\alpha h\nu)^2$, where α is the absorption coefficient and $h\nu$ the photon energy. However, the choice of fitting range of the spectra is widespread; in general, the wider the fitting range is, the larger the derived gaps are. Trapalis *et al.* developed a similar argument and found that the extrapolated band gap can also be varied when adopting the Cody plot with an expression of $(\alpha/h\nu)^2$ [36].

Although we still cannot decisively conclude the origins of larger gaps observed in Zn_3N_2, we hope our calculations and discussion help further experimental analyses.

IV. CONCLUSIONS

In this paper, we investigate the zinc nitride Zn_3N_2 using the HSE06 hybrid functional, which has been reported to accurately predict the band gaps of semiconductors, especially nitrides. First, we show the calculated density of states and band structure and find that the band gap is 0.84 eV in a direct-type band structure. We then discuss the

relation between the electron carrier concentration and the optical gap. The result indicates that the reported optical gaps between 1 and 2 eV can be mainly attributed to the BM effect. Furthermore, the parabolic approximation used for analyzing the BM shift is found to not work well for Zn_3N_2. Second, we assess thermodynamic stability of Zn_3N_2 using the ideal-gas model in conjunction with the rigid-rotor model for gas phases and first-principles phonon calculations for solid phases. It is found that Zn_3N_2 is slightly unstable with respect to the Zn metal and N_2 gas phases at $p_{N_2} = 10^5$ Pa at low temperature and becomes less stable at increased temperature. Third, carrier generation and compensation by native point defects and unintentionally introduced oxygen and hydrogen impurities are discussed. The results suggest that the BM shift occurs even without intentional donor doping due to oxygen substitutions on nitrogen sites and/or hydrogen interstitials. However, reported gaps larger than 2.0 eV are not due to the BM shift because of the Fermi-level pinning caused by zinc vacancies and hydrogen-on-zinc impurities. We also discuss details of peculiar defects such as nitrogen interstitials and nitrogen-on-zinc antisites with N_2 molecularlike or azidelike atomic and electronic structures. Finally, we develop an argument for the possible origins of reported optical gaps larger than 2.0 eV; the likely cause is the choice of the range of absorption spectra used for the Tauc plots.

ACKNOWLEDGMENTS

This work was supported by the MEXT Elements Strategy Initiative to Form Core Research Center, Grants-in-Aid for Young Scientists A (Grant No. 15H05541) and Scientific Research A (Grant No. 17H01318) from JSPS, and the PRESTO (JPMJPR16N4) and Support Program for Starting Up Innovation Hub MI^{2}I from JST, Japan. The computing resources of ACCMS at Kyoto University were used for some of this work.

APPENDIX: ENERGY CORRECTIONS FOR POINT DEFECTS

Here, we address errors in defect-formation energies caused by finite sizes of supercells, and also how accurately they are corrected using *a posteriori* electrostatics-based corrections. More details are discussed in Ref. [47].

Our extension to the FNV correction scheme uses a static dielectric tensor, namely, the sum of the ion-clamped dielectric tensor (ϵ^{ele}) and the ionic contribution (ϵ^{ion}), to account for electrostatic-potential screening [47]. For the test calculations using PBE + U [64,78], we obtain them using density-functional perturbation theory [79,80]. The electronic part includes local-field effects. In cubic systems, only one diagonal component is independent. The calculated ϵ^{ele} and ϵ^{ion} using PBE + U ($U_{eff} = 5$ eV) are 8.30 and 14.60, respectively. In the HSE06 defect calculations, we use the summation of the electronic part calculated using the HSE06 functional and the ionic part calculated using PBE + U at the HSE06 theoretical structure. This approximation is justified because the ionic contributions are determined from the zone-center phonon frequencies and the Born effective charges [81], both of which are expected to be nearly the same between the HSE06 and PBE + U calculations at the same lattice constant. ϵ^{ele} using the HSE06 functional with a finite-electric-field approach is 7.29, which is slightly smaller than the PBE + U value due to the increase of the band gap, whereas ϵ^{ion} from PBE + U is $\epsilon^{ion} = 17.14$.

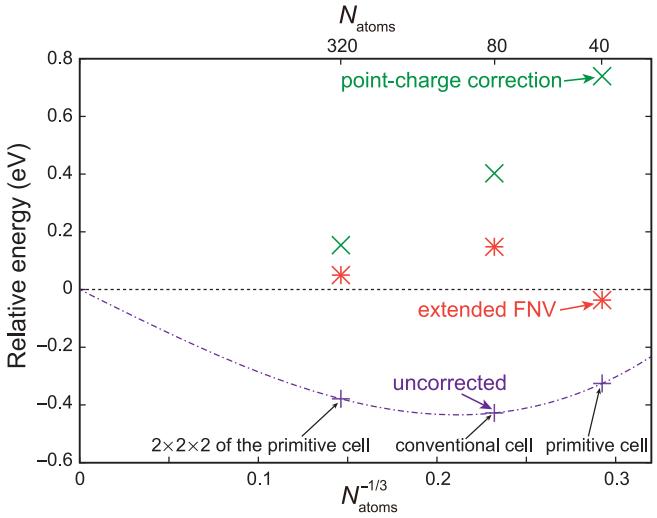

FIG. 11. Uncorrected, point-charge-corrected, and extended FNV-corrected relative defect-formation energies of V_N^{3+} in Zn_3N_2 as a function of the inverse of the cube root of the number of atoms (N_{atoms}). Calculations are performed using PBE + U, and $2 \times 2 \times 2$ MP k-point sampling is adopted. The zero of the relative energies is set to the extrapolated value of the infinite interdefect distance limit by fitting the defect-formation energies with a function of $aN_{atoms}^{-1} + bN_{atoms}^{-1/3} + c$. The upper values are the numbers of atoms in the supercells before vacancy introduction.

Figure 11 presents the relative formation energies of V_N^{3+} in Zn_3N_2 with no corrections, point-charge corrections, and extended FNV corrections as a function of supercell sizes. V_N^{3+} has the largest absolute charge state, and it is expected to have the largest error in this study. One can see that, while the point-charge corrections largely overestimate the defect formation energies, especially at smaller cells, the FNV corrections drastically improve the energies; the remaining error is less than 0.05 eV—even with a 40-atom primitive cell. Therefore, we adopt the primitive cell for defect calculations. We should emphasize that Zn $3d$ orbitals are treated as valence electrons; therefore, the number of valence electrons in the primitive cell amounts to 368, which is computationally demanding when adopting the HSE06 functional.

[1] J. Robertson and S. J. Clark, Limits to doping in oxides, Phys. Rev. B **83**, 075205 (2011).

[2] A. Zakutayev, Design of nitride semiconductors for solar energy conversion, J. Mater. Chem. A **4**, 6742 (2016).

[3] Y. Inoue, M. Nomiya, and O. Takai, Physical properties of reactive sputtered tin-nitride thin films, Vacuum **51**, 673 (1998).

[4] C. M. Caskey, J. A. Seabold, V. Stevanovic, M. Ma, W. A. Smith, D. S. Ginley, N. R. Neale, R. M. Richards, S. Lany, and A. Zakutayev, Semiconducting properties of spinel tin nitride and other IV_3N_4 polymorphs, J. Mater. Chem. C **3**, 1389 (2015).

[5] A. Ziani, E. Nurlaela, D. S. Dhawale, D. A. Silva, E. Alarousu, O. F. Mohammed, and K. Takanabe, Carrier dynamics of a visible-light-responsive Ta_3N_5 photoanode for water oxidation, Phys. Chem. Chem. Phys. **17**, 2670 (2015).

[6] A. N. Fioretti, A. Zakutayev, H. Moutinho, C. Melamed, J. D. Perkins, A. G. Norman, M. Al-Jassim, E. S. Toberer, and A. C. Tamboli, Combinatorial insights into doping control and transport properties of zinc tin nitride, J. Mater. Chem. C **3**, 11017 (2015).

[7] H. Amano, Nobel lecture: Growth of GaN on sapphire via low-temperature deposited buffer layer and realization of *p*-type GaN by Mg doping followed by low-energy electron beam irradiation, Rev. Mod. Phys. **87**, 1133 (2015).

[8] I. Akasaki, Nobel lecture: Fascinated journeys into blue light, Rev. Mod. Phys. **87**, 1119 (2015).

[9] S. Nakamura, Nobel lecture: Background story of the invention of efficient blue InGaN light emitting diodes, Rev. Mod. Phys. **87**, 1139 (2015).

[10] K. Matsuzaki, T. Okazaki, Y.-S. Lee, H. Hosono, and T. Susaki, Controlled bipolar doping in Cu_3N (100) thin films, Appl. Phys. Lett. **105**, 222102 (2014).

[11] L. Lahourcade, N. C. Coronel, K. T. Delaney, S. K. Shukla, N. A. Spaldin, and H. A. Atwater, Structural and optoelectronic characterization of RF sputtered $ZnSnN_2$, Adv. Mater. **25**, 2562 (2013).

[12] Y. Hinuma, T. Hatakeyama, Y. Kumagai, L. A. Burton, H. Sato, Y. Muraba, S. Iimura, H. Hiramatsu, I. Tanaka, H. Hosono, and F. Oba, Discovery of earth-abundant nitride semiconductors by computational screening and high-pressure synthesis, Nat. Commun. **7**, 11962 (2016).

[13] D. Partin, D. Williams, and M. O'Keeffe, The crystal structures of Mg_3N_2 and Zn_3N_2, J. Solid State Chem. **132**, 56 (1997).

[14] M. Futsuhara, K. Yoshioka, and O. Takai, Structural, electrical and optical properties of zinc nitride thin films prepared by reactive RF magnetron sputtering, Thin Solid Films **322**, 274 (1998).

[15] P. Wu, T. Tiedje, H. Alimohammadi, V. Bahrami-Yekta, M. Masnadi-Shirazi, and C. Wang, Molecular beam epitaxy growth and optical properties of single crystal Zn_3N_2 films, Semicond. Sci. Technol. **31**, 10LT01 (2016).

[16] T. Suda and K. Kakishita, Band-gap energy and electron effective mass of polycrystalline Zn_3N_2, J. Appl. Phys. **99**, 076101 (2006).

[17] X. Cao, Y. Yamaguchi, Y. Ninomiya, and N. Yamada, Comparative study of electron transport mechanisms in epitaxial and polycrystalline zinc nitride films, J. Appl. Phys. **119**, 025104 (2016).

[18] X. Cao, A. Sato, Y. Ninomiya, and N. Yamada, Oxygen-doped zinc nitride as a high-mobility nitride-based semiconductor, J. Phys. Chem. C **119**, 5327 (2015).

[19] C. G. Núñez, J. L. Pau, E. Ruiz, and J. Piqueras, Thin film transistors based on zinc nitride as a channel layer for optoelectronic devices, Appl. Phys. Lett. **101**, 253501 (2012).

[20] N. Pereira, L. C. Klein, and G. G. Amatucci, The electrochemistry of Zn_3N_2 and LiZnN a lithium reaction mechanism for metal nitride electrodes, J. Electrochem. Soc. **149**, A262 (2002).

[21] N. H. Erdogan, K. Kara, H. Ozdamar, R. Esen, and H. Kavak, Effect of the oxidation temperature on microstructure and conductivity of Zn_xN_y thin films and their conversion into *p*-type ZnO:N films, Appl. Surf. Sci. **271**, 70 (2013).

[22] R. Ayouchi, C. Casteleiro, L. Santos, and R. Schwarz, RF-plasma assisted PLD growth of Zn_3N_2 thin films, Phys. Status Solidi (c) **7**, 2294 (2010).

[23] S. R. Bhattacharyya, R. Ayouchi, M. Pinnisch, and R. Schwarz, Transfer characteristic of zinc nitride based thin film transistors, Phys. Status Solidi (c) **9**, 469 (2012).

[24] T. Oshima and S. Fujita, (111)-oriented Zn_3N_2 growth on *a*-plane sapphire substrates by molecular beam epitaxy, Jpn. J. Appl. Phys. **45**, 8653 (2006).

[25] E. Maile and R. Fischer, MOCVD of the cubic zinc nitride phase, Zn_3N_2, using $Zn[N(SiMe_3)_2]_2$ and ammonia as precursors, Chem. Vap. Deposition **11**, 409 (2005).

[26] K. Toyoura, H. Tsujimura, T. Goto, K. Hachiya, R. Hagiwara, and Y. Ito, Optical properties of zinc nitride formed by molten salt electrochemical process, Thin Solid Films **492**, 88 (2005).

[27] M. Futsuhara, K. Yoshioka, and O. Takai, Structural, electrical and optical properties of zinc nitride thin films prepared by reactive RF magnetron sputtering, Thin Solid Films **322**, 274 (1998).

[28] C. G. Núñez, J. L. Pau, M. J. Hernández, M. Cervera, E. Ruiz, and J. Piqueras, On the zinc nitride properties and the unintentional incorporation of oxygen, Thin Solid Films **520**, 1924 (2012).

[29] F. Zong, H. Ma, W. Du, J. Ma, X. Zhang, H. Xiao, F. Ji, and C. Xue, Optical band gap of zinc nitride films prepared on quartz substrates from a zinc nitride target by reactive RF magnetron sputtering, Appl. Surf. Sci. **252**, 7983 (2006).

[30] T. Yang, Z. Zhang, Y. Li, M. Lv, S. Song, Z. Wu, J. Yan, and S. Han, Structural and optical properties of zinc nitride films prepared by RF magnetron sputtering, Appl. Surf. Sci. **255**, 3544 (2009).

[31] K. Kuriyama, Y. Takahashi, and F. Sunohara, Optical band gap of Zn_3N_2 films, Phys. Rev. B **48**, 2781 (1993).

[32] F. Zong, H. Ma, C. Xue, H. Zhuang, X. Zhang, H. Xiao, J. Ma, and F. Ji, Synthesis and thermal stability of Zn_3N_2 powder, Solid State Commun. **132**, 521 (2004).

[33] G. Paniconi, Z. Stoeva, R. I. Smith, P. C. Dippo, B. L. Gallagher, and D. H. Gregory, Synthesis, stoichiometry and thermal stability of Zn_3N_2 powders prepared by ammonolysis reactions, J. Solid State Chem. **181**, 158 (2008).

[34] D. D. Wagman, W. Evans, V. Parker, R. H. Schumm, I.Halow, S. M. Bailey, K. L. Churney, and R. L. Nuttall, The NBS tables of chemical thermodynamic properties: Selected values for inorganic and C_1 and C_2 organic substances in SI units, J. Phys. Chem. Ref. Data **11**, 1 (1982).

[35] G. Z. Xing, D. D. Wang, B. Yao, L. F. N. A. Qune, T. Yang, Q. He, J. H. Yang, and L. L. Yang, Structural and electrical characteristics of high quality (100) orientated-Zn_3N_2 thin films grown by radio-frequency magnetron sputtering, J. Appl. Phys. **108**, 083710 (2010).

[36] A. Trapalis, J. Heffernan, I. Farrer, J. Sharman, and A. Kean, Structural, electrical, and optical characterization of as grown and oxidized zinc nitride thin films, J. Appl. Phys. **120**, 205102 (2016).

[37] W. Walukiewicz, J. W. Ager III, K. M. Yu, Z. Liliental-Weber, J. Wu, S. X. Li, R. E. Jones, and J. D. Denlinger, Structure and electronic properties of InN and In-rich group III-nitride alloys, J. Phys. D **39**, R83 (2006).

[38] J. Wu, W. Walukiewicz, S. X. Li, R. Armitage, J. C. Ho, E. R. Weber, E. E. Haller, H. Lu, W. J. Schaff, A. Barcz, and R. Jakiela, Effects of electron concentration on the optical absorption edge of InN, Appl. Phys. Lett. **84**, 2805 (2004).

[39] P. Rinke, M. Scheffler, A. Qteish, M. Winkelnkemper, D. Bimberg, and J. Neugebauer, Band gap and band parameters of InN and GaN from quasiparticle energy calculations based on exact-exchange density-functional theory, Appl. Phys. Lett. **89**, 161919 (2006).

[40] R. Deng, B. D. Ozsdolay, P. Y. Zheng, S. V. Khare, and D. Gall, Optical and transport measurement and first-principles determination of the ScN band gap, Phys. Rev. B **91**, 045104 (2015).

[41] E. Burstein, Anomalous optical absorption limit in InSb, Phys. Rev. **93**, 632 (1954).

[42] T. S. Moss, The interpretation of the properties of indium antimonide, Proc. Phys. Soc. London Sect. B **67**, 775 (1954).

[43] R. Long, Y. Dai, L. Yu, B. Huang, and S. Han, Atomic geometry and electronic structure of defects in Zn_3N_2, Thin Solid Films **516**, 1297 (2008).

[44] R. Long, Y. Dai, L. Yu, M. Guo, and B. Huang, Structural, electronic, and optical properties of oxygen defects in Zn_3N_2, J. Phys. Chem. B **111**, 3379 (2007).

[45] N. Jiang, J. L. Roehl, S. V. Khare, D. G. Georgiev, and A. H. Jayatissa, An *ab initio* computational study of pure Zn_3N_2 and its native point defects and dopants Cu, Ag and Au, Thin Solid Films **564**, 331 (2014).

[46] C. G. Van de Walle and J. Neugebauer, First-principles calculations for defects and impurities: Applications to III-nitrides, J. Appl. Phys. **95**, 3851 (2004).

[47] Y. Kumagai and F. Oba, Electrostatics-based finite-size corrections for first-principles point defect calculations, Phys. Rev. B **89**, 195205 (2014).

[48] P. E. Blöchl, Projector augmented-wave method, Phys. Rev. B **50**, 17953 (1994).

[49] G. Kresse and J. Furthmüller, Efficient iterative schemes for *ab initio* total-energy calculations using a plane-wave basis set, Phys. Rev. B **54**, 11169 (1996).

[50] G. Kresse and D. Joubert, From ultrasoft pseudopotentials to the projector augmented-wave method, Phys. Rev. B **59**, 1758 (1999).

[51] J. Heyd, G. E. Scuseria, and M. Ernzerhof, Hybrid functionals based on a screened Coulomb potential, J. Chem. Phys. **118**, 8207 (2003).

[52] J. Heyd, G. E. Scuseria, and M. Ernzerhof, Erratum: Hybrid functionals based on a screened Coulomb potential, J. Chem. Phys. **124**, 219906(E) (2006).

[53] A. V. Krukau, O. A. Vydrov, A. F. Izmaylov, and G. E. Scuseria, Influence of the exchange screening parameter on the performance of screened hybrid functionals, J. Chem. Phys. **125**, 224106 (2006).

[54] Y. Kumagai, Y. Soda, F. Oba, A. Seko, and I. Tanaka, First-principles calculations of the phase diagrams and band gaps in $CuInSe_2$-$CuGaSe_2$ and $CuInSe_2$-$CuAlSe_2$ pseudobinary systems, Phys. Rev. B **85**, 033203 (2012).

[55] S.-H. Yoo, A. Walsh, D. O. Scanlon, and A. Soon, Electronic structure and band alignment of zinc nitride, Zn_3N_2, RSC Adv. **4**, 3306 (2014).

[56] D. O. Scanlon, C. W. Dunnill, J. Buckeridge, S. A. Shevlin, A. J. Logsdail, S. M. Woodley, C. R. A. Catlow, M. J. Powell, R. G. Palgrave, I. P. Parkin, G. W. Watson, T. W. Keal, P. Sherwood, A. Walsh, and A. A. Sokol, Band alignment of rutile and anatase TiO_2, Nat. Mater. **12**, 798 (2013).

[57] Y. K. Frodason, K. M. Johansen, T. S. Bjørheim, B. G. Svensson, and A. Alkauskas, Zn vacancy as a polaronic hole trap in ZnO, Phys. Rev. B **95**, 094105 (2017).

[58] Y. Kumagai, M. Choi, Y. Nose, and F. Oba, First-principles study of point defects in chalcopyrite $ZnSnP_2$, Phys. Rev. B **90**, 125202 (2014).

[59] M. Choi, F. Oba, Y. Kumagai, and I. Tanaka, Antiferrodistortive-like oxygen-octahedron rotation induced by the oxygen vacancy in cubic $SrTiO_3$, Adv. Mater. **25**, 86 (2013).

[60] A. Janotti, J. B. Varley, P. Rinke, N. Umezawa, G. Kresse, and C. G. Van de Walle, Hybrid functional studies of the oxygen vacancy in TiO_2, Phys. Rev. B **81**, 085212 (2010).

[61] D. A. McQuarrie and J. D. Simon, *Physical Chemistry: A Molecular Approach* (University Science Books, Mill Valley, CA, 1997).

[62] M. T. Dove, *Introduction to Lattice Dynamics* (Cambridge University Press, Cambridge, England, 1993).

[63] J. P. Perdew, A. Ruzsinszky, G. I. Csonka, O. A. Vydrov, G. E. Scuseria, L. A. Constantin, X. Zhou, and K. Burke, Restoring the Density-Gradient Expansion for Exchange in Solids and Surfaces, Phys. Rev. Lett. **100**, 136406 (2008).

[64] S. L. Dudarev, G. A. Botton, S. Y. Savrasov, C. J. Humphreys, and A. P. Sutton, Electron-energy-loss spectra and the structural stability of nickel oxide: An LSDA + U study, Phys. Rev. B **57**, 1505 (1998).

[65] A. Togo and I. Tanaka, First principles phonon calculations in materials science, Scr. Mater. **108**, 1 (2015).

[66] C. Freysoldt, J. Neugebauer, and C. G. Van de Walle, Fully *Ab Initio* Finite-Size Corrections for Charged-Defect Supercell Calculations, Phys. Rev. Lett. **102**, 016402 (2009).

[67] Y. Kumagai, L. A. Burton, A. Walsh, and F. Oba, Electronic structure and defect physics of tin sulfides: SnS, Sn_2S_3, and SnS_2, Phys. Rev. Applied **6**, 014009 (2016).

[68] H.-P. Komsa, T. T. Rantala, and A. Pasquarello, Finite-size supercell correction schemes for charged defect calculations, Phys. Rev. B **86**, 045112 (2012).

[69] Y. Hinuma, G. Pizzi, Y. Kumagai, F. Oba, and I. Tanaka, Band structure diagram paths based on crystallography, Comput. Mater. Sci. **128**, 140 (2017).
[70] X. Cao, Y. Ninomiya, and N. Yamada, Zinc nitride as a potential high-mobility transparent conductor, Physica Status Solidi (A) **214**, 1600472 (2017).
[71] H. J. Monkhorst and J. D. Pack, Special points for Brillouin-zone integrations, Phys. Rev. B **13**, 5188 (1976).
[72] A. Janotti, J. L. Lyons, and C. G. Van de Walle, Hybrid functional calculations of native point defects in InN, Phys. Status Solidi (a) **209**, 65 (2012).
[73] S. Lany and A. Zunger, Anion vacancies as a source of persistent photoconductivity in II–VI and chalcopyrite semiconductors, Phys. Rev. B **72**, 035215 (2005).
[74] F. Oba, A. Togo, I. Tanaka, J. Paier, and G. Kresse, Defect energetics in ZnO: A hybrid Hartree-Fock density functional study, Phys. Rev. B **77**, 245202 (2008).
[75] R. D. Shannon, Revised effective ionic radii and systematic studies of interatomic distances in halides and chalcogenides, Acta Crystallogr. Sect. A **32**, 751 (1976).
[76] S. Kirklin, J. E. Saal, B. Meredig, A. Thompson, J. W. Doak, M. Aykol, S. Rühl, and C. Wolverton, The Open Quantum Materials Database (OQMD): Assessing the accuracy of DFT formation energies, npj Comput. Mater. **1**, 15010 (2015).
[77] C. G. Van de Walle, J. L. Lyons, and A. Janotti, Controlling the conductivity of InN, Phys. Status Solidi (a) **207**, 1024 (2010).
[78] J. P. Perdew, K. Burke, and M. Ernzerhof, Generalized Gradient Approximation Made Simple, Phys. Rev. Lett. **77**, 3865 (1996).
[79] S. Baroni and R. Resta, *Ab initio* calculation of the macroscopic dielectric constant in silicon, Phys. Rev. B **33**, 7017 (1986).
[80] M. Gajdoš, K. Hummer, G. Kresse, J. Furthmüller, and F. Bechstedt, Linear optical properties in the projector-augmented wave methodology, Phys. Rev. B **73**, 045112 (2006).
[81] E. Cockayne and B. P. Burton, Phonons and static dielectric constant in $CaTiO_3$ from first principles, Phys. Rev. B **62**, 3735 (2000).